Spiral Spin Liquid on a Honeycomb Lattice

Shang Gao,[1,2,*] Michael A. McGuire,[2] Yaohua Liu,[1] Douglas L. Abernathy,[1] Clarina dela Cruz,[1] Matthias Frontzek,[1] Matthew B. Stone,[1] and Andrew D. Christianson[2]

[1]*Neutron Scattering Division, Oak Ridge National Laboratory, Oak Ridge, Tennessee 37831, USA*

[2]*Materials Science & Technology Division, Oak Ridge National Laboratory, Oak Ridge, Tennessee 37831, USA*

(Received 23 November 2021; revised 18 January 2022; accepted 25 March 2022; published 1 June 2022)

Spiral spin liquids are correlated paramagnetic states with degenerate propagation vectors forming a continuous ring or surface in reciprocal space. On the honeycomb lattice, spiral spin liquids present a novel route to realize emergent fracton excitations, quantum spin liquids, and topological spin textures, yet experimental realizations remain elusive. Here, using neutron scattering, we show that a spiral spin liquid is realized in the van der Waals honeycomb magnet $FeCl_3$. A continuous ring of scattering is directly observed, which indicates the emergence of an approximate U(1) symmetry in momentum space. Our work demonstrates that spiral spin liquids can be achieved in two-dimensional systems and provides a promising platform to study the fracton physics in spiral spin liquids.

DOI: 10.1103/PhysRevLett.128.227201

Similar to geometrical frustration [1,2], competition among interactions at different length scales is able to induce novel electronic or magnetic states regardless of the lattice geometry. A representative example is the spiral spin liquid (SSL), which is a type of classical spin liquid realized on a bipartite lattice [3–20]. In such a state, spins fluctuate collectively as spirals, and their propagation vectors, $\boldsymbol{q}$, form a continuous ring or surface in reciprocal space. Depending on the specific shape of the spiral surface, the low-energy fluctuations in a SSL may behave as topological vortices in momentum space, leading to an effective tensor gauge theory with highly unconventional fracton quadrupole excitations [20–23]. Such nonlocal dynamics is very different from that in geometrically frustrated magnets, where the elementary excitations are local spin flips. Compared to the conventional frustrated geometry, a bipartite lattice offers more flexibility on the signs of the interactions, as the duality between antiferromagnetic and ferromagnetic interactions indicates that a SSL can be realized even in ferromagnets as long as sufficient competition exists [3]. Since degeneracy enhances quantum fluctuations [2,24], the SSL has thus been proposed as a novel route to realize quantum spin liquids in systems dominated by ferromagnetic interactions [5–9]. Furthermore, when perturbations, e.g., the further-neighbor interactions or anisotropic interactions, induce a magnetic long-range order, degeneracy in the SSL may be partially retained, leading to skyrmionlike topological spin textures [25–27] that have great potential for applications in spintronic devices [28,29].

On a bipartite lattice with Heisenberg interactions, a SSL emerges when the ratio between the effective second-neighbor and first-neighbor couplings $|J_2^*/J_1|$ is higher than a threshold of $1/(2Z)$, where Z counts the number of the nearest-neighboring sites [3,8]. Depending on the exact lattice geometry, J_2^* may include contributions from further-neighbor interactions at fixed ratios [8,13,20]. However, on the honeycomb or diamond lattice where the sum of two successive J_1 paths always equals a J_2 path [3,5], further-neighbor contributions to J_2^* are not necessary to stabilize a SSL ($J_2^* = J_2$), which greatly simplifies the experimental realization. The phase diagram of a J_1-J_2 model on a honeycomb lattice [5] is summarized in Fig. 1, where the evolution of the representative $\boldsymbol{q} = (q, q, 0)$ over the degenerate ground state manifold is shown explicitly. Following the definition of the spiral surface on the diamond lattice [3], we call the degenerate ring in the SSL state a *spiral ring*. Above the threshold of $|J_2/J_1| = 1/6$, the ferromagnetic (FM, $J_1 < 0$) or Néel ($J_1 > 0$) state with $q = 0$ is replaced by a SSL state with nonzero q, and the spiral ring gradually transforms from a circular shape around the Brillouin zone center Γ, into triangular lobes centered on the $K\{\frac{1}{3}, \frac{1}{3}\}$ points as $|J_2/J_1|$ increases. The case with a spiral ring around Γ is extremely interesting, as the low-energy dynamics can be described as fracton quadrupoles in a rank-2 U(1) tensor gauge theory [20], which is a heavily investigated field with deep connections to quantum information, elasticity, and gravity [22,23,30–33].

In spite of the elegant simplicity of the theoretical model, experimental realization of a SSL is challenging as J_2 is often relatively weak in real materials [25,34–41]. To our knowledge, $MnSc_2S_4$ has remained as the only host of a SSL on the diamond lattice [25], while the feasibility of realizing a SSL on the honeycomb lattice is still unclear. Here we show that a SSL state with an approximate U(1) symmetry in momentum space is realized in the

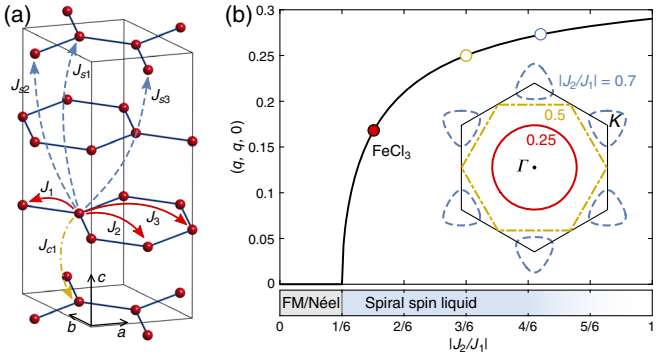

FIG. 1. (a) The Fe^{3+} ions ($S = 5/2$) in $FeCl_3$ form honeycomb lattices with ABC-type stacking along the c axis. Red solid arrows indicate the nearest-, second-, and third-neighbor couplings J_1, J_2, and J_3, respectively. Yellow dot-dashed arrow indicates the interlayer couplings J_{c1}. Blue dashed arrows indicate the second-layer couplings J_{s1}, J_{s2}, and J_{s3}. (b) A SSL state is realized on the honeycomb lattice at $|J_2/J_1| > 1/6$ (blue shaded in the bottom panel) with propagation vectors forming a continuous ring in reciprocal space, which we refer to as the spiral ring. The black curve in the top panel shows the position of a representative propagation vector $(q, q, 0)$ over the spiral ring as a function of $|J_2/J_1|$. Inset shows the complete spiral rings at $|J_2/J_1| = 0.25$, 0.5, and 0.7 as indicated by circular markers over the black curve. The red filled marker indicates the location of $FeCl_3$ with an effective ratio of $|J_2/J_1| \sim 0.25$ as determined from the J_1-J_2-J_c minimal model (see text).

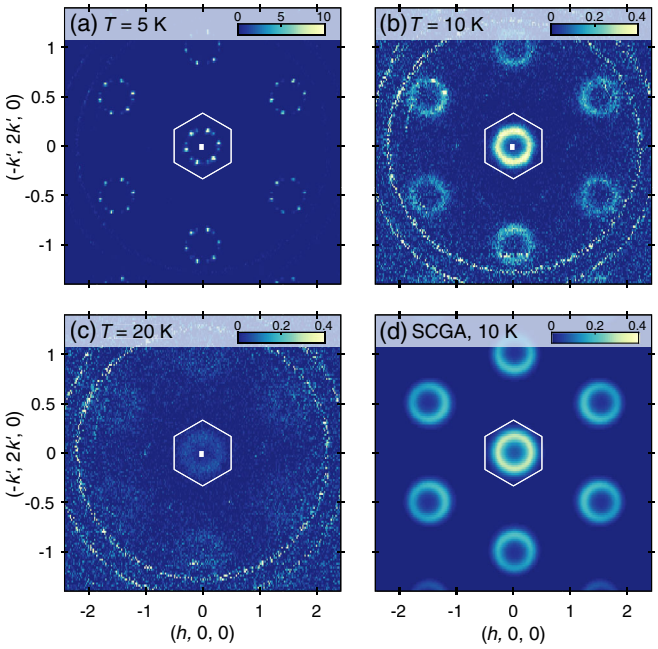

FIG. 2. (a)–(c) Temperature evolution of the quasi-elastic spin correlations in the $l = -1.5$ plane measured on CORELLI at $T = 5$, 10, and 20 K. The white hexagon outlines the first nuclear Brillouin zone. Data are integrated in the range of $l = [-1.6, -1.4]$. Measurements at 50 K have been subtracted as the background. In (b) and (c), the double rings spanning the whole panel are background scattering from the sample environment, which is less evident in (a) due to the different intensity scale. (d) Calculated diffuse neutron scattering pattern in the $l = -1.5$ plane using the minimal J_1-J_2-J_{c1} model at $T = 10$ K. The coupling strengths are $J_1 = -0.3$, $J_2 = 0.075$, and $J_{c1} = 0.15$ meV. Variations in coupling strengths do not qualitatively affect the diffuse pattern as long as $J_2/J_1 = -0.25$ with J_1 and J_{c1} being ferromagnetic and antiferromagnetic, respectively.

honeycomb magnet $FeCl_3$ [42–47]. This compound belongs to the van der Waals trihalide family that has recently attracted great attention for its fundamental and application interests [48–50]. As shown in Fig. 1(a), the honeycomb Fe^{3+} ($S = 5/2$) layers in $FeCl_3$ are ABC stacked along the c axis, leading to a rhombohedral $R\bar{3}$ space group. Previous neutron diffraction experiments performed in the 1960s [42,43] revealed a helical magnetic long-range order (LRO) with $\boldsymbol{q} = (\frac{4}{15}, \frac{1}{15}, \frac{3}{2})$ below the transition temperature $T_N \sim 10$ K, which indicates an antiferromagnetic interlayer alignment and possible intralayer frustration. In the present Letter, we utilize state-of-the-art neutron scattering measurements to study the short-range spin correlations above T_N. A continuous ring of scattering around Γ is observed, which provides direct evidence for the existence of a SSL state with an approximate U(1) symmetry in momentum space. The spiral correlations can be mainly ascribed to the J_1-J_2 competition, which is further corroborated through inelastic neutron scattering (INS) in the long-range ordered phase. Details for sample preparations and neutron scattering experiments are presented in the Supplemental Material [34], which includes additional Refs. [51–71].

Diffuse neutron scattering probes the short-range spin correlations in reciprocal space. Figures 2(a)–2(c) summarize the temperature dependence of our diffuse scattering pattern in the $l = -1.5$ plane, as it exhibits the strongest intensity throughout reciprocal space. Below the transition temperature of $T_N \sim 8$ K, magnetic Bragg peaks belonging to $\boldsymbol{q} = (\frac{4}{15}, \frac{1}{15}, \frac{3}{2})$ are observed, which is consistent with the previous diffraction study [42]. At 10 K above T_N, the magnetic Bragg peaks merge together, leading to a ring of scattering that implies an emergent U(1) symmetry in momentum space [20]. This scattering ring can be discerned at temperatures up to ∼20 K as shown in Fig. 2(c), indicating a relatively wide stability regime for the spiral correlations.

To confirm that the diffuse ring of scattering originates from a SSL state, we calculate the short-range spin correlations using the self-consistent Gaussian approximation (SCGA) method [34]. The fact that the diffuse scattering intensity at 10 K is concentrated in the half integer l planes suggests antiferromagnetic correlations between the neighboring honeycomb layers. Therefore, in addition to the J_1 and J_2 interactions within the honeycomb layers, we consider an antiferromagnetic interlayer interaction J_{c1} along the c axis as shown in Fig. 1(a).

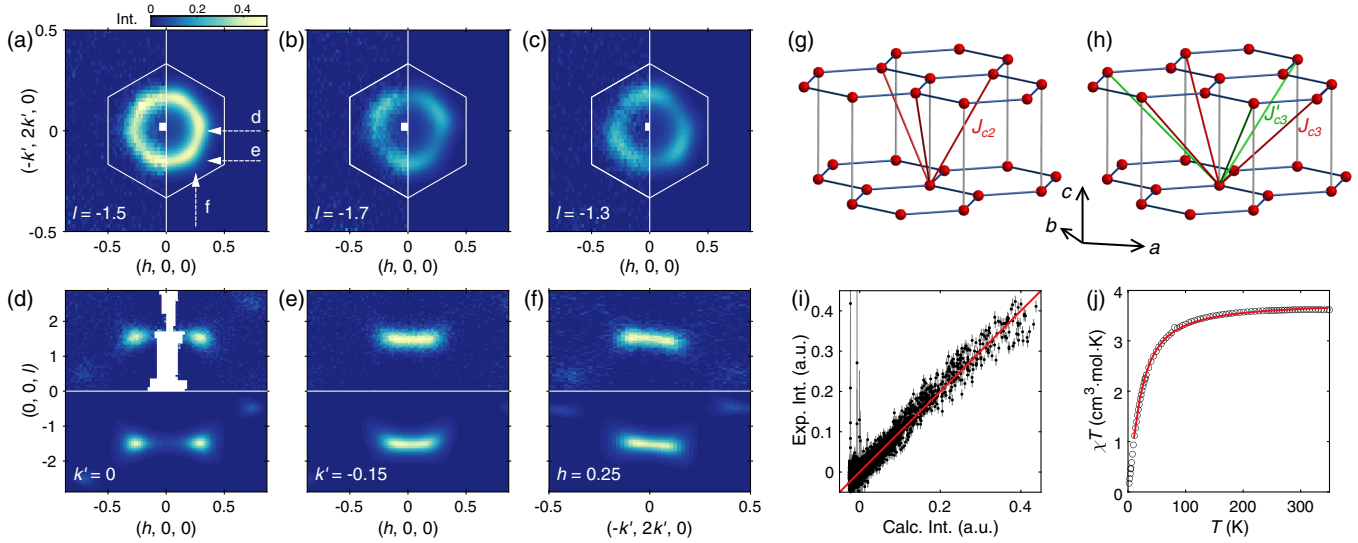

FIG. 3. (a)–(f) Diffuse neutron scattering intensity measured at 10 K together with the simulated results. Data in the $l = -1.5$, -1.7, and -1.3 planes are shown in the left half of panels (a)–(c), respectively. Data in the $k' = 0$, $k' = -0.15$, and $h = 0.25$ planes are shown in the upper half of panels (d)–(f), respectively. In panels (a)–(c), the white hexagon outlines the first nuclear Brillouin zone. Dashed arrows in panel (a) indicate the directions of the vertical slices in panels (d)–(f). (g),(h) Exchange paths for the interlayer interactions (g) J_{c2} (red solid line) and (h) J_{c3} (red solid line). In panel (h), the J'_{c3} interactions (green solid line) are symmetrically inequivalent with the J_{c3} interactions in spite of their equal distances. (i) Comparison of the experimental and calculated diffuse scattering intensities using the J_{123}-J_{c123} model. The fitted coupling strengths are $J_1 = -0.249(4)$, $J_2 = 0.089(1)$, $J_3 = 0.026(1)$, $J_{c1} = 0.019(9)$, $J_{c2} = 0.042(2)$, $J_{c3} = 0.030(2)$ meV. Uncertainties are estimated from 50 independent runs. The goodness-of-fit factor is $\chi^2 = 1.77$. (j) Temperature dependence of the reduced magnetic susceptibility χT (black circle) together with the calculated values based upon the SCGA method described in the text (red line). Data are measured on a powder sample in a 1 T magnetic field [34]. Error bars representing the standard deviations are smaller than the symbols.

With ferromagnetic J_1 and a frustration ratio of $J_2/J_1 = -0.25$, the calculated pattern presented in Fig. 2(d) captures the scattering ring observed at $T = 10$ K, thus establishing the existence of an intrinsic SSL state in $FeCl_3$. The effective ratio of $|J_2/J_1| = 0.25$ also grants a good approximation of the U(1) symmetry in reciprocal space since higher ratios may introduce a strong distortion of the circular shape as compared in Fig. 1(b).

Although the J_1-J_2-J_{c1} minimal model successfully reproduces the spiral ring in the $l = -1.5$ plane, it is too simplified to describe the full spin correlations in $FeCl_3$. Figures 3(a)–3(f) summarize the detailed intensity distribution of the spiral ring. The corresponding data in a wider range are shown in the Supplemental Material [34]. The scattering intensity on the two sides of the $l = -1.5$ plane exhibits reversed three-fold symmetry patterns, which is not reproduced by the J_1-J_2-J_{c1} model [34] and suggests a weak U(1) symmetry breaking due to further perturbations.

Using the SCGA method, we explore the effects on the spiral ring from perturbations that are allowed by the $R\bar{3}$ symmetry. As discussed in the Supplemental Material [34], perturbations from the anisotropic interactions including the Kitaev-like interactions or the relativistic Dzyaloshinskii-Moriya (DM) interactions are not able to reproduce the diffuse scattering data. Therefore, we concentrate on the isotropic further-neighbor interactions that are consistent with the quenched orbital degree of freedom of the Fe^{3+} ions. Besides the third-neighbor coupling J_3 within the honeycomb layer shown in Fig. 1(a), two additional interlayer couplings J_{c2} and J_{c3} are found to be important in explaining the diffuse scattering data. Figures 3(g) and 3(h) present the exchange paths for the J_{c2} and J_{c3} interactions. The J_{c3} interaction couples the spin at the origin to those at $\boldsymbol{a} + \boldsymbol{c}/3$ and the equivalent positions, where $\boldsymbol{a}$ and $\boldsymbol{c}$ are the basis vectors of the hexagonal unit cell. This interaction should be differentiated from the equal-distant J'_{c3} interaction shown by the green solid lines in Fig. 3(h), as their exchange paths are subject to different symmetry constraints. Using the combined simplex and simulated annealing optimization method [72], we fit the diffuse scattering data over volumes of reciprocal space together with the temperature dependence of the magnetic susceptibility $\chi(T)$. The fitted results are presented in Figs. 3(i) and 3(j) for the volume diffuse scattering data and the reduced magnetic susceptibility, respectively, and the fitted diffuse patterns are presented in Figs. 3(a)–3(f) together with the experimental results. The fitted coupling strengths as listed in the caption of Fig. 3 reveal a relatively high frustration ratio of $|J_2/J_1| = 0.36$, thus confirming the J_1-J_2 competition as the driving force of the SSL state in $FeCl_3$.

Greater insight into the spin interactions emerges through the analysis of the spin excitations. Figure 4(a) summarizes

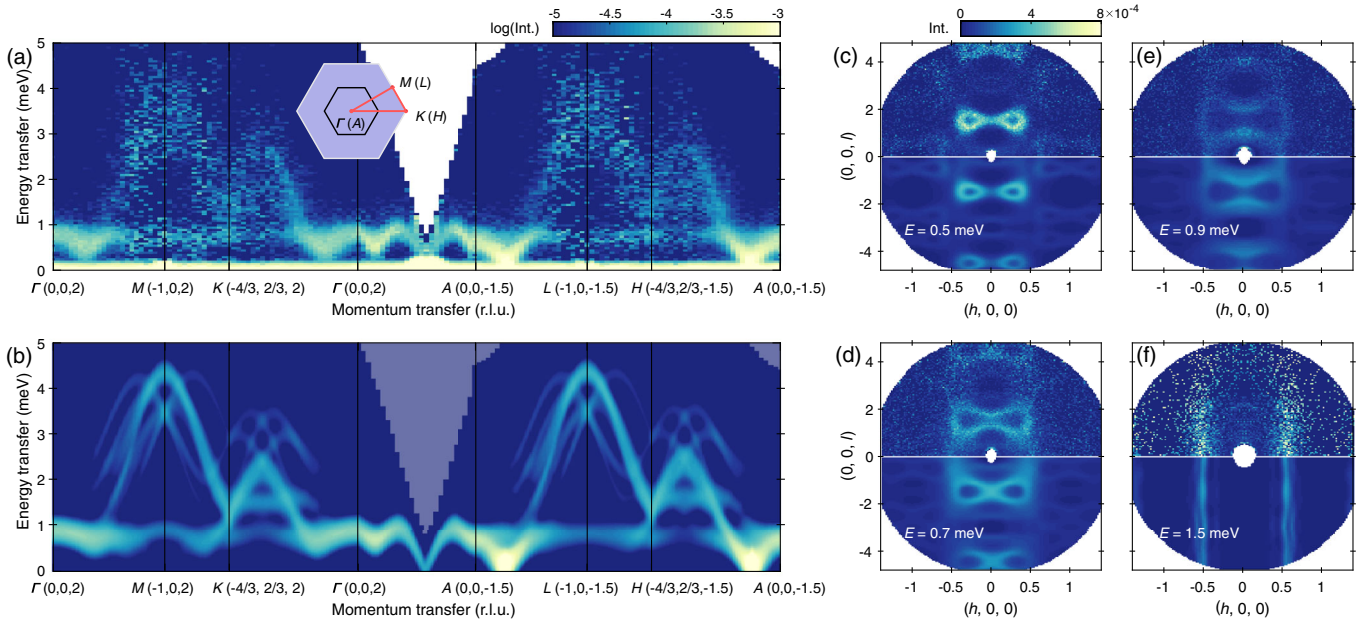

FIG. 4. (a) Experimental INS spectra $S(\boldsymbol{Q},\omega)$ measured on SEQUOIA with an incident neutron energy of $E_i = 8$ meV at $T = 4$ K along the high symmetry directions. Data are symmetrized according to the $R\bar{3}$ symmetry. The positions of the high symmetry points in the $l = 2$ and $l = -1.5$ planes are shown in the inset, with the first nuclear Brillouin zone being outlined by the black hexagon. Intensity is plotted in a log scale. (b) Calculated INS spectra using the linear spin wave theory for a J_{123}-J_{c123}-J_{s123} model with fitted coupling strengths of $J_1 = -0.28(3), J_2 = 0.095(9), J_3 = 0.008(5), J_{c1} = 0.05(3), J_{c2} = 0.024(5), J_{c3} = 0.026(6), J_{s1} = 0.01(1), J_{s2} = -0.007(3)$, and $J_{s3} = -0.003(4)$ meV. Uncertainties are estimated from 20 independent runs. A weak easy plane single-ion anisotropy of 1 μeV is included to stabilize the helical ground state. The calculated spectra are convoluted by a Gaussian function with a fitted full-width at half-maximum (FWHM) of 0.35 meV. Intensity is plotted in a log scale as that for the experimental data. (c–f) Comparison between the experimental and calculated constant-energy slices at $E = 0.5$ (c), 0.7 (d), 0.9 (e), and 1.5 (f) meV. Data are integrated in an energy range of ± 0.1 meV. Intensity in panel (f) is multiplied by 8 times for better visibility. The same linear intensity scale as shown in panel (c) is utilized for panels (c-f).

the INS spectra $S(\boldsymbol{Q},\omega)$ of $FeCl_3$ measured at $T = 5$ K in the helical ordered phase. Magnon excitations emanating from the LRO $\boldsymbol{q} = (\frac{4}{15}, \frac{1}{15}, \frac{3}{2})$ are observed throughout reciprocal space. Two magnon branches can be discerned in the energy ranges of [0, 1.0] and [1.0, 4.0] meV, which can be correspondingly attributed to the in-phase and anti-phase movements of the two sublattice spins on the honeycomb lattice. The gapless excitations along the A-L-H-A line in the $l = -1.5$ plane are consistent with the ground state degeneracy caused by the J_1-J_2 competition. Compared to the instrumental resolution of ~0.19 meV at the elastic line, the observed magnons, especially the [1.0, 4.0] meV branch, exhibit a broader width, up to ~1 meV, indicating unresolved magnon modes due to multiple magnetic domains together with the separated $\boldsymbol{Q} \pm \boldsymbol{q}$ excitations [58]. In contrast, all these modes overlap along the c axis, which leads to a better-resolved gull wing-shaped dispersion along the Γ-A line.

To understand the spin excitations in $FeCl_3$, we perform linear spin wave calculations for the Heisenberg spin Hamiltonian. As discussed in the Supplemental Material [34], the J_{123}-J_{c123} model captures the main features of the magnon dispersion in the honeycomb layers but produces a dispersion along the c axis that is clearly weaker than the observed spectrum. Therefore, three additional couplings J_{s1}, J_{s2}, and J_{s3} are included in the spin Hamiltonian, which are the shortest exchange interactions between the second-neighboring layers as shown in Fig. 1(a). By fitting the INS spectra at $E < 1.0$ meV, we arrive at the parameter set listed in the caption of Fig. 4. The strengths of the second-layer couplings are relatively weak as expected from their longer exchange paths, and the strengths of the remaining interlayer and intralayer couplings are close to those fitted from the J_{123}-J_{s123} model. The calculated INS spectra in Fig. 4(b) reproduce the experimental data, and the good agreement is further confirmed through the comparison of the experimental and calculated constant energy slices shown in Figs. 4(c)–4(f). Meanwhile, the calculated diffuse scattering patterns for the J_{123}-J_{c123}-J_{s123} model stay almost unchanged [34], suggesting that short-range spin correlations are not sensitive to the weak second-layer interactions.

The perturbations on the minimal J_1-J_2-J_{c1} model also explain the selection of the LRO $\boldsymbol{q}$ position over the spiral ring. Using the Luttinger-Tisza method [8], the ground state of the J_1-J_2-J_{c1} model can be calculated to be a spiral with $\boldsymbol{q} = (\frac{1}{6}, \frac{1}{6}, \frac{3}{2})$, while the LRO $\boldsymbol{q}$ of the perturbed J_{123}-J_{c123}-J_{s123} model become (0.194,0.096,1.5), which

is closer to the experimentally observed value of $\boldsymbol{q} = (\frac{4}{15}, \frac{1}{15}, \frac{3}{2})$. Although fine-tuning of the coupling strengths seems necessary to exactly reproduce the commensurate $\boldsymbol{q}$ position in $FeCl_3$, theoretical calculations of SSLs have proposed a lock-in mechanism where an incommensurate $\boldsymbol{q}$ becomes pinned to a nearby commensurate position due to weak single-ion anisotropy and crystal symmetry [4,34]. Such a lock-in mechanism may account for the commensurate $\boldsymbol{q}$ position in $FeCl_3$.

Our experimental study on $FeCl_3$ demonstrates that SSLs can be realized in two-dimensional systems. Remarkably, the observed spiral ring around Γ implies an emergent U(1) symmetry in momentum space and establishes $FeCl_3$ as a promising platform to study the fracton gauge theory. This prospect is further encouraged because $FeCl_3$ can be easily cleaved into monolayers, allowing for the elimination of the out-of-plane perturbations, J_c and J_s. The discovery of a SSL in $FeCl_3$ also motivates further investigations of quantum spin liquids and topological spin textures on the honeycomb lattice. Current experimental endeavors on quantum spin liquids are mainly focused on the Kitaev approach [49], while the approach via the SSL phase has remained barely explored [8,73]. Knowing the origin of the relatively high ratio of $|J_2/J_1|$ in $FeCl_3$, e.g., through the *ab initio* calculations, will help discover more SSL hosts on the honeycomb lattice and facilitate the tuning of SSL towards the quantum limit or spintronics applications [74–77].

We acknowledge helpful discussions with Cheng-Long Zhang at RIKEN CEMS. This work was supported by the U.S. Department of Energy, Office of Science, Basic Energy Sciences, Materials Sciences and Engineering Division. This research used resources at the Spallation Neutron Source (SNS) and the High Flux Isotope Reactor (HFIR), both are DOE Office of Science User Facilities operated by the Oak Ridge National Laboratory (ORNL).

*sgao.physics@gmail.com

[1] Steven T. Bramwell and Michel J. P. Gingras, Spin ice state in frustrated magnetic pyrochlore materials, Science **294**, 1495 (2001).
[2] Leon Balents, Spin liquids in frustrated magnets, Nature (London) **464**, 199 (2010).
[3] Doron Bergman, Jason Alicea, Emanuel Gull, Simon Trebst, and Leon Balents, Order-by-disorder and spiral spin-liquid in frustrated diamond-lattice antiferromagnets, Nat. Phys. **3**, 487 (2007).
[4] SungBin Lee and Leon Balents, Theory of the ordered phase in *a*-site antiferromagnetic spinels, Phys. Rev. B **78**, 144417 (2008).
[5] A. Mulder, R. Ganesh, L. Capriotti, and A. Paramekanti, Spiral order by disorder and lattice nematic order in a frustrated Heisenberg antiferromagnet on the honeycomb lattice, Phys. Rev. B **81**, 214419 (2010).
[6] G. Chen, M. Hermele, and L. Radzihovsky, Frustrated Quantum Critical Theory of Putative Spin-Liquid Phenomenology in $6H$-B-$Ba_3NiSb_2O_9$, Phys. Rev. Lett. **109**, 016402 (2012).
[7] Hao Zhang and C. A. Lamas, Exotic disordered phases in the quantum J_1-J_2 model on the honeycomb lattice, Phys. Rev. B **87**, 024415 (2013).
[8] Nils Niggemann, Max Hering, and Johannes Reuther, Classical spiral spin liquids as a possible route to quantum spin liquids, J. Phys. Condens. Matter **32**, 024001 (2020).
[9] Rico Pohle, Han Yan, and Nic Shannon, Theory of $Ca_{10}Cr_7O_{28}$ as a bilayer breathing-kagome magnet: Classical thermodynamics and semiclassical dynamics, Phys. Rev. B **104**, 024426 (2021).
[10] Jan Attig and Simon Trebst, Classical spin spirals in frustrated magnets from free-fermion band topology, Phys. Rev. B **96**, 085145 (2017).
[11] Yasir Iqbal, Tobias Müller, Harald O. Jeschke, Ronny Thomale, and Johannes Reuther, Stability of the spiral spin liquid in $MnSc_2S_4$, Phys. Rev. B **98**, 064427 (2018).
[12] Péter Balla, Yasir Iqbal, and Karlo Penc, Degenerate manifolds, helimagnets, and multi-q chiral phases in the classical Heisenberg antiferromagnet on the face-centered-cubic lattice, Phys. Rev. Research **2**, 043278 (2020).
[13] Péter Balla, Yasir Iqbal, and Karlo Penc, Affine lattice construction of spiral surfaces in frustrated Heisenberg models, Phys. Rev. B **100**, 140402(R) (2019).
[14] Gang Chen, Quantum paramagnet and frustrated quantum criticality in a spin-one diamond lattice antiferromagnet, Phys. Rev. B **96**, 020412(R) (2017).
[15] Tokuro Shimokawa and Hikaru Kawamura, Ripple State in the Frustrated Honeycomb-Lattice Antiferromagnet, Phys. Rev. Lett. **123**, 057202 (2019).
[16] Xu-Ping Yao, Jian Qiao Liu, Chun-Jiong Huang, Xiaoqun Wang, and Gang Chen, Generic spiral spin liquids, Front. Phys. **16**, 53303 (2021).
[17] Chun-Jiong Huang, Jian Qiao Liu, and Gang Chen, Versatility of spiral spin liquid in frustrated van der Waals magnets, Phys. Rev. Research **4**, 013121 (2022).
[18] Finn Lasse Buessen, Max Hering, Johannes Reuther, and Simon Trebst, Quantum Spin Liquids in Frustrated Spin-1 Diamond Antiferromagnets, Phys. Rev. Lett. **120**, 057201 (2018).
[19] Jian Qiao Liu, Fei-Ye Li, Gang Chen, and Ziqiang Wang, Featureless quantum paramagnet with frustrated criticality and competing spiral magnetism on spin-1 honeycomb lattice magnet, Phys. Rev. Research **2**, 033260 (2020).
[20] Han Yan and Johannes Reuther, companion article, Low-energy structure of spiral spin liquids, Phys. Rev. Research **4**, 023175 (2022).
[21] Michael Pretko, Subdimensional particle structure of higher rank U(1) spin liquids, Phys. Rev. B **95**, 115139 (2017).
[22] Rahul M. Nandkishore and Michael Hermele, Fractons, Annu. Rev. Condens. Matter Phys. **10**, 295 (2019).
[23] Michael Pretko, Xie Chen, and Yizhi You, Fracton phases of matter, Int. J. Mod. Phys. A **35**, 2030003 (2020).
[24] Yi Zhou, Kazushi Kanoda, and Tai-Kai Ng, Quantum spin liquid states, Rev. Mod. Phys. **89**, 025003 (2017).
[25] Shang Gao, Oksana Zaharko, Vladimir Tsurkan, Yixi Su, Jonathan S. White, Gregory S. Tucker, Bertrand Roessli,

Frederic Bourdarot, Romain Sibille, Dmitry Chernyshov, Tom Fennell, Alois Loidl, and Christian Rüegg, Spiral spin-liquid and the emergence of a vortex-like state in $MnSc_2S_4$, Nat. Phys. **13**, 157 (2017).

[26] Shang Gao, H. Diego Rosales, Flavia A. Gómez Albarracín, Vladimir Tsurkan, Guratinder Kaur, Tom Fennell, Paul Steffens, Martin Boehm, Petr Čermák, Astrid Schneidewind, Eric Ressouche, Daniel C. Cabra, Christian Rüegg, and Oksana Zaharko, Fractional antiferromagnetic skyrmion lattice induced by anisotropic couplings, Nature (London) **586**, 37 (2020).

[27] Tokuro Shimokawa, Tsuyoshi Okubo, and Hikaru Kawamura, Multiple-q states of the J_1-J_2 classical honeycomb-lattice Heisenberg antiferromagnet under a magnetic field, Phys. Rev. B **100**, 224404 (2019).

[28] Naoto Nagaosa and Yoshinori Tokura, Topological properties and dynamics of magnetic skyrmions, Nat. Nanotechnol. **8**, 899 (2013).

[29] Albert Fert, Nicolas Reyren, and Vincent Cros, Magnetic skyrmions: Advances in physics and potential applications, Nat. Rev. Mater. **2**, 17031 (2017).

[30] Michael Pretko, Emergent gravity of fractons: Mach's principle revisited, Phys. Rev. D **96**, 024051 (2017).

[31] Gábor B. Halász, Timothy H. Hsieh, and Leon Balents, Fracton Topological Phases from Strongly Coupled Spin Chains, Phys. Rev. Lett. **119**, 257202 (2017).

[32] Michael Pretko and Leo Radzihovsky, Fracton-Elasticity Duality, Phys. Rev. Lett. **120**, 195301 (2018).

[33] Han Yan, Hyperbolic fracton model, subsystem symmetry, and holography, Phys. Rev. B **99**, 155126 (2019).

[34] See Supplemental Material at http://link.aps.org/supplemental/10.1103/PhysRevLett.128.227201 for details on sample preparations, magnetization measurements, neutron scattering experiments, data analyses, and model comparisons.

[35] G. J. MacDougall, A. A. Aczel, Yixi Su, W. Schweika, E. Faulhaber, A. Schneidewind, A. D. Christianson, J. L. Zarestky, H. D. Zhou, D. Mandrus, and S. E. Nagler, Revisiting the ground state of $CoAl_2O_4$: Comparison to the conventional antiferromagnet $MnAl_4O_4$, Phys. Rev. B **94**, 184422 (2016).

[36] L. Ge, J. Flynn, J. A. M. Paddison, M. B. Stone, S. Calder, M. A. Subramanian, A. P. Ramirez, and M. Mourigal, Spin order and dynamics in the diamond-lattice Heisenberg antiferromagnets $CuRh_2O_4$ and $CoRh_2O_4$, Phys. Rev. B **96**, 064413 (2017).

[37] J. R. Chamorro, L. Ge, J. Flynn, M. A. Subramanian, M. Mourigal, and T. M. McQueen, Frustrated spin one on a diamond lattice in $NiRh_2O_4$, Phys. Rev. Mater. **2**, 034404 (2018).

[38] Vladimir Tsurkan, Hans-Albrecht Krug von Nidda, Joachim Deisenhofer, Peter Lunkenheimer, and Alois Loidl, On the complexity of spinels: Magnetic, electronic, and polar ground states, Phys. Rep. **926**, 1 (2021).

[39] Yuya Haraguchi, Kazuhiro Nawa, Chishiro Michioka, Hiroaki Ueda, Akira Matsuo, Koichi Kindo, Maxim Avdeev, Taku J. Sato, and Kazuyoshi Yoshimura, Frustrated magnetism in the J_1-J_2 honeycomb lattice compounds $MgMnO_3$ and $ZnMnO_3$ synthesized via a metathesis reaction, Phys. Rev. Mater. **3**, 124406 (2019).

[40] Aly H. Abdeldaim, Teng Li, Lewis Farrar, Alexander A. Tsirlin, Wenjiao Yao, Alexandra S. Gibbs, Pascal Manuel, Philip Lightfoot, Gøran J. Nilsen, and Lucy Clark, Realizing square and diamond lattice $S = 1/2$ Heisenberg antiferromagnet models in the α and β phases of the coordination framework, $KTi(C_2O_4)_2 \cdot H_2O$, Phys. Rev. Mater. **4**, 104414 (2020).

[41] Akihiro Otsuka, Yasuhiro Shimizu, Gunzi Saito, Mitsuhiko Maesato, Andhika Kiswandhi, Takaaki Hiramatsu, Yukihiro Yoshida, Hideki Yamochi, Masahisa Tsuchiizu, Yuto Nakamura, Hideo Kishida, and Hiroshi Ito, Canting antiferromagnetic spin-order ($T_N = 102$ K) in a monomer Mott insulator $(ET)Ag_4(CN)_5$ with a diamond spin-lattice, Bull. Chem. Soc. Jpn. **93**, 260 (2020).

[42] J. W. Cable, M. K. Wilkinson, E. O. Wollan, and W. C. Koehler, Neutron-diffraction study of antiferromagnetic $FeCl_3$, Phys. Rev. **127**, 714 (1962).

[43] Edwin R. Jones, O. B. Morton, L. Cathey, Theo Auel, and E. L. Amma, Low-temperature magnetic susceptibility of $FeCl_3$, J. Chem. Phys. **50**, 4755 (1969).

[44] J. P. Stampfel, W. T. Oosterhuis, B. Window, and F. deS. Barros, Mössbauer-effect measurements in antiferromagnetic $FeCl_3$, Phys. Rev. B **8**, 4371 (1973).

[45] P. B. Johnson, S. A. Friedberg, and J. A. Rayne, Field-induced magnetic phase transitions in $FeCl_3$, J. Appl. Phys. **52**, 1932 (1981).

[46] S. Hashimoto, K. Forster, and S. C. Moss, Structure refinement of an $FeCl_3$ crystal using a thin plate sample, J. Appl. Crystallogr. **22**, 173 (1989).

[47] Byeongki Kang, Changsoo Kim, Euna Jo, Sangil Kwon, and Soonchil Lee, Magnetic state of $FeCl_3$ investigated by NMR, J. Magn. Magn. Mater. **360**, 1 (2014).

[48] Bevin Huang, Genevieve Clark, Efrén Navarro-Moratalla, Dahlia R. Klein, Ran Cheng, Kyle L. Seyler, Ding Zhong, Emma Schmidgall, Michael A. McGuire, David H. Cobden, Wang Yao, Di Xiao, Pablo Jarillo-Herrero, and Xiaodong Xu, Layer-dependent ferromagnetism in a van der Waals crystal down to the monolayer limit, Nature (London) **546**, 270 (2017).

[49] Arnab Banerjee, Jiaqiang Yan, Johannes Knolle, Craig A. Bridges, Matthew B. Stone, Mark D. Lumsden, David G. Mandrus, David A. Tennant, Roderich Moessner, and Stephen E. Nagler, Neutron scattering in the proximate quantum spin liquid α-$RuCl_3$, Science **356**, 1055 (2017).

[50] Michael A. McGuire, Crystal and magnetic structures in layered, transition metal dihalides and trihalides, Crystals **7**, 121 (2017).

[51] Andrew F May, Jiaqiang Yan, and Michael A McGuire, A practical guide for crystal growth of van der Waals layered materials, J. Appl. Phys. **128**, 051101 (2020).

[52] C. Starr, F. Bitter, and A. R. Kaufmann, The magnetic properties of the iron group anhydrous chlorides at low temperatures. I. Experimental, Phys. Rev. **58**, 977 (1940).

[53] M. D. Frontzek, R. Whitfield, K. M. Andrews, A. B. Jones, M. Bobrek, K. Vodopivec, B. C. Chakoumakos, and J. A. Fernandez-Baca, Wand^2—A versatile wide angle neutron powder/single crystal diffractometer, Rev. Sci. Instrum. **89**, 092801 (2018).

[54] J. Rodriguez-Carvajal, Recent advances in magnetic structure determination by neutron powder diffraction, Physica (Amsterdam) **192B**, 55 (1993).
[55] Feng Ye, Yaohua Liu, Ross Whitfield, Ray Osborn, and Stephan Rosenkranz, Implementation of cross correlation for energy discrimination on the time-of-flight spectrometer CORELLI, J. Appl. Crystallogr. **51**, 315 (2018).
[56] O. Arnold *et al.*, Mantid—Data analysis and visualization package for neutron scattering and μSR experiments, Nucl. Instrum. Methods Phys. Res., Sect. A **764**, 156 (2014).
[57] R. A. Ewings, A. Buts, M. D. Le, J. van Duijn, I. Bustinduy, and T. G. Perring, Horace: Software for the analysis of data from single crystal spectroscopy experiments at time-of-flight neutron instruments, Nucl. Instrum. Methods Phys. Res., Sect. A **834**, 132 (2016).
[58] S. Toth and B. Lake, Linear spin wave theory for single-Q incommensurate magnetic structures, J. Phys. Condens. Matter **27**, 166002 (2015).
[59] R. D. Johnson, S. C. Williams, A. A. Haghighirad, J. Singleton, V. Zapf, P. Manuel, I. I. Mazin, Y. Li, H. O. Jeschke, R. Valentí, and R. Coldea, Monoclinic crystal structure of α-$RuCl_3$ and the zigzag antiferromagnetic ground state, Phys. Rev. B **92**, 235119 (2015).
[60] Tai Kong, Shu Guo, Danrui Ni, and Robert J. Cava, Crystal structure and magnetic properties of the layered van der Waals compound VBr_3, Phys. Rev. Mater. **3**, 084419 (2019).
[61] P. H. Conlon and J. T. Chalker, Absent pinch points and emergent clusters: Further neighbor interactions in the pyrochlore Heisenberg antiferromagnet, Phys. Rev. B **81**, 224413 (2010).
[62] Joseph A. M. Paddison, Scattering Signatures of Bond-Dependent Magnetic Interactions, Phys. Rev. Lett. **125**, 247202 (2020).
[63] Shang Gao, Vilmos Kocsis, Minoru Soda, Feng Ye, Yaohua Liu, Andrew F. May, Yasujiro Taguchi, Yoshinori Tokura, Taka-hisa Arima, Werner Schweika, Andrew D. Christianson, and Matthew B. Stone, Suppressed incommensurate order in swedenborgite $Ca_{0.5}Y_{0.5}BaCo_4O_7$, Phys. Rev. B **104**, L140408 (2021).
[64] Matthew Enjalran and Michel J. P. Gingras, Theory of paramagnetic scattering in highly frustrated magnets with long-range dipole-dipole interactions: The case of the $Tb_2Ti_2O_7$ pyrochlore antiferromagnet, Phys. Rev. B **70**, 174426 (2004).
[65] Jeffrey G. Rau, Eric Kin-Ho Lee, and Hae-Young Kee, Generic Spin Model for the Honeycomb Iridates Beyond the Kitaev Limit, Phys. Rev. Lett. **112**, 077204 (2014).
[66] Lebing Chen, Jae-Ho Chung, Bin Gao, Tong Chen, Matthew B. Stone, Alexander I. Kolesnikov, Qingzhen Huang, and Pengcheng Dai, Topological Spin Excitations in Honeycomb Ferromagnet CrI_3, Phys. Rev. X **8**, 041028 (2018).
[67] M. Matsuda, S. E. Dissanayake, D. L. Abernathy, Y. Qiu, J. R. D. Copley, N. Kumada, and M. Azuma, Frustrated magnetic interactions in an $S = 3/2$ bilayer honeycomb lattice compound $Bi_3Mn_4O_{12}$ (NO_3), Phys. Rev. B **100**, 134430 (2019).
[68] Christian Wessler, Bertrand Roessli, Karl W. Krämer, Bernard Delley, Oliver Waldmann, Lukas Keller, Denis Cheptiakov, Hans B. Braun, and Michel Kenzelmann, Observation of plaquette fluctuations in the spin-1/2 honeycomb lattice, npj Quantum Mater. **5**, 85 (2020).
[69] Fengfeng Zhu, Lichuan Zhang, Xiao Wang, Flaviano José dos Santos, Junda Song, Thomas Mueller, Karin Schmalzl, Wolfgang F. Schmidt, Alexandre Ivanov, Jitae T. Park, Jianhui Xu, Jie Ma, Samir Lounis, Stefan Blügel, Yuriy Mokrousov, Yixi Su, and Thomas Brückel, Topological magnon insulators in two-dimensional van der Waals ferromagnets $CrSiTe_3$ and $CrGeTe_3$: Toward intrinsic gap-tunability, Sci. Adv. **7**, eabi7532 (2021).
[70] Zhengwei Cai, Song Bao, Zhao-Long Gu, Yi-Peng Gao, Zhen Ma, Yanyan Shangguan, Wenda Si, Zhao-Yang Dong, Wei Wang, Yizhang Wu, Dongjing Lin, Jinghui Wang, Kejing Ran, Shichao Li, Devashibhai Adroja, Xiaoxiang Xi, Shun-Li Yu, Xiaoshan Wu, Jian-Xin Li, and Jinsheng Wen, Topological magnon insulator spin excitations in the two-dimensional ferromagnet $CrBr_3$, Phys. Rev. B **104**, L020402 (2021).
[71] Lebing Chen, Matthew B. Stone, Alexander I Kolesnikov, Barry Winn, Wonhyuk Shon, Pengcheng Dai, and Jae-Ho Chung, Massless Dirac magnons in the two dimensional van der Waals honeycomb magnet $CrCl_3$, 2D Mater. **9**, 015006 (2022).
[72] E. Farhi, Y. Debab, and P. Willendrup, iFit: A new data analysis framework. Applications for data reduction and optimization of neutron scattering instrument simulations with McStas, J. Neutron Res. **17**, 5 (2014).
[73] Shou-Shu Gong, D. N. Sheng, Olexei I. Motrunich, and Matthew P. A. Fisher, Phase diagram of the spin-$\frac{1}{2}$ J_1-J_2 Heisenberg model on a honeycomb lattice, Phys. Rev. B **88**, 165138 (2013).
[74] V. Baltz, A. Manchon, M. Tsoi, T. Moriyama, T. Ono, and Y. Tserkovnyak, Antiferromagnetic spintronics, Rev. Mod. Phys. **90**, 015005 (2018).
[75] T. Jungwirth, J. Sinova, A. Manchon, X. Marti, J. Wunderlich, and C. Felser, The multiple directions of antiferromagnetic spintronics, Nat. Phys. **14**, 200 (2018).
[76] Xiaobo Lu, Ruixiang Fei, Linghan Zhu, and Li Yang, Meron-like topological spin defects in monolayer $CrCl_3$, Nat. Commun. **11**, 4724 (2020).
[77] Mathias Augustin, Sarah Jenkins, Richard F. L. Evans, Kostya S. Novoselov, and Elton J. G. Santos, Properties and dynamics of meron topological spin textures in the two-dimensional magnet $CrCl_3$, Nat. Commun. **12**, 185 (2021).